



# Dual-polarity pulse processing and analysis for charge-loss correction in cadmium–zinc–telluride pixel detectors

Leonardo Abbene,<sup>a,\*</sup> Gaetano Gerardi,<sup>a</sup> Fabio Principato,<sup>a</sup> Manuele Bettelli,<sup>b</sup> Paul Seller,<sup>c</sup> Matthew C. Veale,<sup>c</sup> Oliver Fox,<sup>d</sup> Kawal Sawhney,<sup>d</sup> Nicola Zambelli,<sup>e</sup> Giacomo Benassi<sup>e</sup> and Andrea Zappettini<sup>b</sup>

Received 28 February 2018

Accepted 26 April 2018

Edited by P. A. Pianetta, SLAC National Accelerator Laboratory, USA

**Keywords:** X-ray and gamma-ray detectors; CdZnTe detectors; charge sharing; charge losses; energy-resolved photon-counting detectors.

<sup>a</sup>Dipartimento di Fisica e Chimica, University of Palermo, Viale delle Scienze, Edificio 18, Palermo 90128, Italy,

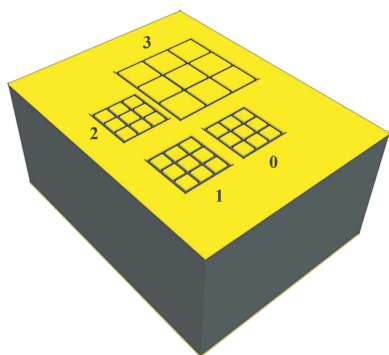
<sup>b</sup>IMEM/CNR, Parco Area delle Scienze 37/A, Parma 43100, Italy, <sup>c</sup>Science and Technology Facilities Council, Rutherford Appleton Laboratory, Chilton, Oxfordshire OX11 0QX, UK, <sup>d</sup>B16 Beamline, Diamond Light Source, Fermi Avenue, Didcot, UK, and <sup>e</sup>due2lab s.r.l., Via Paolo Borsellino 2, Scandiano, Reggio Emilia 42019, Italy.

\*Correspondence e-mail: leonardo.abbene@unipa.it

Charge losses at the inter-pixel gap are typical drawbacks in cadmium–zinc–telluride (CZT) pixel detectors. In this work, an original technique able to correct charge losses occurring after the application of charge-sharing addition (CSA) is presented. The method, exploiting the strong relation between the energy after CSA and the beam position at the inter-pixel gap, allows the recovery of charge losses and improvements in energy resolution. Sub-millimetre CZT pixel detectors were investigated with both uncollimated radiation sources and collimated synchrotron X-rays, at energies below and above the *K*-shell absorption energy of the CZT material. The detectors are DC coupled to fast and low-noise charge-sensitive preamplifiers (PIXIE ASIC) and followed by a 16-channel digital readout electronics, performing multi-parameter analysis (event arrival time, pulse shape, pulse height). Induced-charge pulses with negative polarity were also observed in the waveforms from the charge-sensitive preamplifiers (CSPs) at energies >60 keV. The shape and the height of these pulses were analysed, and their role in the mitigation of charge losses in CZT pixel detectors. These activities are in the framework of an international collaboration on the development of energy-resolved photon-counting systems for spectroscopic X-ray imaging (5–140 keV).

## 1. Introduction

In the last two decades, CdTe (cadmium telluride) and CZT (cadmium–zinc–telluride) arrays with sub-millimetre pixelization have been widely proposed for the development of room-temperature energy-resolved photon-counting (ERPC) systems (Abbene *et al.*, 2015*a*; Barber *et al.*, 2015; Del Sordo *et al.*, 2004; Iwanczyk *et al.*, 2009; Meuris *et al.*, 2009; Seller *et al.*, 2011; Szeles *et al.*, 2008; Zhang *et al.*, 2007). ERPC systems, due to their single-photon-counting and energy-resolving capabilities, have opened new perspectives in several application areas such as synchrotron science, homeland security, medical imaging and astrophysics (Ballabriga *et al.*, 2016; Green *et al.*, 2016; Iniewski, 2014; Norlin *et al.*, 2008; Taguchi & Iwanczyk, 2013; Tomita *et al.*, 2004). As is well known (Barrett *et al.* 1995; Eskin *et al.*, 1999; Mardor *et al.*, 2001; He, 2001), CdTe/CZT detectors with pixelated anodes are characterized by electron-sensing properties (small pixel effect), which are very important to minimize the spectral distortions related to the poor hole transport properties of CdTe/CZT materials (Del Sordo *et al.*, 2009; Owens & Peacock, 2004). This effect is



due to the particular shape of the weighting potential of a collecting pixel: it is low near the cathode and monotonically rises rapidly close to the anode. Therefore, in agreement with the Shockley–Ramo theorem (He, 2001; Knoll, 2000; Ramo, 1939; Shockley, 1938), the charge induced on a collecting pixel, proportional to the weighting potential, is mostly contributed from the drift of charge carriers close to the pixel. By applying negative bias voltages at the cathode, these charge carriers are the electrons and pulses with positive polarity will be generated at the collecting pixel. Moreover, according to the small pixel effect, this unipolar effect is enhanced by decreasing the ratio between the pixel size and the detector thickness.

However, when small pixel arrays are used, the performance is strongly limited by the distortions caused by charge-sharing and cross-talk phenomena (Bolotnikov *et al.*, 2005; Guerra *et al.*, 2008). Generally, charge sharing refers to the splitting of the electron charge cloud generated from a single photon and collected by the neighbouring pixels. The area over which the charge cloud is deposited will depend upon charge diffusion, Coulomb repulsion, *K*-shell X-ray fluorescence and Compton scattering.

Cross-talk events between neighbouring pixels can also be created by *K*-shell X-ray fluorescence (side and back escape events), Compton scattering and by induced-charge pulses (Guerra *et al.*, 2008; Brambilla *et al.*, 2012; Bolotnikov *et al.*, 2016; Kim *et al.*, 2011; Zhu *et al.*, 2011). The induced-charge pulses (or transient pulses) are generated by the movement of the electron cloud over a collecting pixel that will also induce a small signal on the surrounding non-collecting pixels (weighting potential cross-talk). This is due to the particular shape of the weighting potential of a pixel detector, which is characterized by non-zero values even for interaction far from the collecting pixel (Barrett *et al.* 1995; Eskin *et al.*, 1999; Abbene *et al.*, 2018). The induced-charge pulses are fast pulses that in the absence of charge trapping will drop quickly to a zero value. The presence of charge trapping and the different interaction depths of the events can create transient pulses with positive or negative polarities (Budtz-Jørgensen & Kuvvetli, 2017; Eskin *et al.*, 1999; Hong *et al.*, 2006; Zhu *et al.*, 2011). The percentage of charge-sharing and cross-talk events can be very high even for thin detectors. Typically, 2 mm-thick CZT arrays with pixel pitches of 500  $\mu\text{m}$  and 250  $\mu\text{m}$  are characterized by charge-sharing percentages of 60% (500  $\mu\text{m}$  pitch) and 80% (250  $\mu\text{m}$  pitch) at 60 keV (Abbene *et al.*, 2018). The effects of these phenomena on the response of CZT/CdTe pixel detectors have been studied extensively through both theoretical (Chen *et al.*, 2002; Guerra *et al.*, 2008; Iniewski *et al.*, 2007; Xu *et al.*, 2011) and experimental approaches (Brambilla *et al.*, 2012, 2013; Bolotnikov *et al.*, 2016; Frojdh *et al.*, 2011; Kim *et al.*, 2011; Kuvvetli & Budtz-Jørgensen, 2007; Meuris *et al.*, 2009; Veale *et al.*, 2014). Charge sharing and cross-talk can result in degradation of the spectroscopic performance of a pixel detector. These effects can include a worsening of the energy resolution, the introduction of low-energy tailing to photopeaks, the appearance of fluorescence and associated escape peaks and an increase of the low-energy background. They depend on both the physical (electric field,

size and drift of charge cloud, surface conductivity of the inter-pixel gap) and the geometrical features (pixel size, inter-pixel gap, thickness) of the detectors.

Charge-sharing distortions are typically mitigated through the application of charge-sharing discrimination (CSD) techniques, *i.e.* by rejecting the pulses that are in temporal coincidence. These shared events can also be corrected through charge-sharing addition (CSA) techniques, which consist of summing the energies of the coincidence events (Allwork *et al.*, 2012; Kuvvetli & Budtz-Jørgensen, 2007; Meuris *et al.*, 2009; Veale *et al.*, 2014). Unfortunately, the presence of charge losses at the inter-pixel gap has often limited the application of CSA in CdTe/CZT pixel detectors (Abbene *et al.*, 2015a, 2018; Allwork *et al.*, 2012; Brambilla *et al.*, 2012; Bolotnikov *et al.*, 1999, 2002a; Gaskin *et al.*, 2003; Kalemci & Matteson, 2002; Kim *et al.*, 2011; Kuvvetli & Budtz-Jørgensen, 2007). Several interpretations have been given about these charge losses, such as (i) the non-zero energy threshold of the readout electronics (Kalemci & Matteson, 2002), the presence of electric field distortions at the inter-pixel gap (Bolotnikov *et al.*, 1999, 2002a; Kuvvetli & Budtz-Jørgensen, 2007) and the simultaneous presence of both the collected and the induced-charge components in the shared pulses between adjacent pixels (Bolotnikov *et al.*, 2014; Kim *et al.*, 2011). A straightforward mitigation of this problem is often obtained by making the inter-pixel gap as small as possible (Kuvvetli & Budtz-Jørgensen, 2007) or by using steering grids between the pixels (Bolotnikov *et al.*, 2002b; Kim *et al.*, 2011). However, when biased grids are used, the presence of additional surface leakage currents (which increase the electronic noise) and the collecting of some fraction of charges by the same grids can further limit the performance of the detectors.

In this work, we will present an original technique able to correct charge losses at the inter-pixel gap and improve the energy resolution of energy spectra after the application of CSA. CZT pixel arrays, with different geometries and fabricated by various manufactures, were investigated. Charge-sharing measurements were performed with both uncollimated radiation sources ( $^{109}\text{Cd}$  and  $^{241}\text{Am}$  sources) and collimated (10  $\mu\text{m}$   $\times$  10  $\mu\text{m}$ ) synchrotron X-rays, at energies below and above the *K*-shell absorption energy of the CZT material (26.7 keV, 9.7 keV and 31.8 keV for Cd, Zn and Te, respectively).

Induced-charge pulses with negative polarity were also observed in the output waveforms from charge-sensitive preamplifiers (CSPs) at energies  $>60$  keV ( $^{57}\text{Co}$  source). The shape and the height of these pulses were analysed and their role in the mitigation of charge losses in CZT pixel detectors.

## 2. Materials and methods

### 2.1. Detectors

CZT pixel detectors with different anode arrays and thicknesses were fabricated by IMEM-CNR (Parma, Italy; <http://www.imem.cnr.it>) and due2lab s.r.l. (Reggio Emilia, Italy; <http://www.due2lab.com>). The IMEM detectors are

based on CZT crystals ( $4.25 \text{ mm} \times 3.25 \text{ mm} \times 1 \text{ mm}$ ;  $4.25 \text{ mm} \times 3.25 \text{ mm} \times 2 \text{ mm}$ ), grown by Redlen Technologies (Victoria BC, Canada; <http://redlen.ca>) with the travelling heater method (THM) technique (Awadalla *et al.*, 2014; Chen *et al.*, 2007, 2008). In the last decade, spectroscopic-grade CZT crystals with excellent electron charge transport properties ( $\mu_e\tau_e > 10^{-2} \text{ cm}^2 \text{ V}^{-1}$ ;  $\mu_h\tau_h \simeq 10^{-5} \text{ cm}^2 \text{ V}^{-1}$ ) have been routinely produced by Redlen. Gold electroless contacts were realized on both the anode and the cathode of the detectors. A 4%  $\text{AuCl}_3$  methanol solution, with a deposition time of 1 min at  $25^\circ\text{C}$ , was used (Benassi *et al.*, 2017). The anode pattern was obtained by photolithography process and the passivation procedure was performed with an aqueous solution of  $\text{H}_2\text{O}_2$  at 10% for 5 min, in order to reduce the surface leakage currents (Marchini *et al.*, 2009). CZT detectors with gold electroless contacts are routinely fabricated at IMEM-CNR and characterized by low leakage currents at room temperature ( $<5 \text{ nA cm}^{-2}$  at  $1000 \text{ V cm}^{-1}$ ) (Abbene *et al.*, 2016, 2017; Zappettini *et al.*, 2009). As shown in Fig. 1, the anode surface is characterized by four arrays of  $3 \times 3$  pixels with pixel pitches of 500 and 250  $\mu\text{m}$ , surrounded by a guard-ring electrode, while the cathode is a planar electrode covering the detector surface. The width of the inter-pixel gaps for all arrays is equal to 50  $\mu\text{m}$ .

For comparison, a CZT pixel detector (REDLEN detector), fabricated by Redlen Technologies, with the same cathode and anode layout was also investigated. The detector is based on a novel high-flux CZT crystal, recently produced by Redlen Technologies, characterized by enhanced hole charge transport properties ( $\mu_e\tau_e > 10^{-3} \text{ cm}^2 \text{ V}^{-1}$ ;  $\mu_h\tau_h \simeq 10^{-4} \text{ cm}^2 \text{ V}^{-1}$ ) (Iniewski, 2016; Thomas *et al.*, 2017). As is well known, improvements in the charge transport properties of the holes are very important to mitigate the high-flux radiation-induced polarization phenomena in CZT pixel detectors (Abbene *et al.*, 2016; Bale & Szeles, 2008; Sellin *et al.*, 2010).

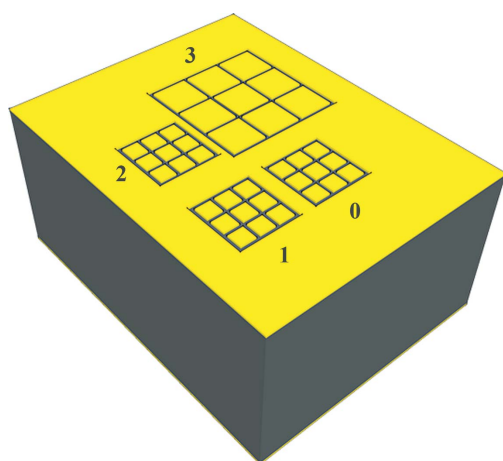


**Figure 1**  
The anode layout of the CZT pixel detectors. The array 3 is characterized by a pixel pitch of 500  $\mu\text{m}$  and the arrays 0, 1, 2 by a pixel pitch of 250  $\mu\text{m}$ . The width of the inter-pixel gaps for all arrays is equal to 50  $\mu\text{m}$ . All arrays are surrounded by a guard-ring electrode up to the edge of the crystal.

## 2.2. Electronics

The detectors are DC coupled to a fast and low-noise ASIC (PIXIE ASIC), developed at Rutherford Appleton Laboratory (Didcot, UK) (Allwork *et al.*, 2012; Veale *et al.*, 2011). The PIXIE ASIC consists of four arrays of  $3 \times 3$  pixels, flip-chip bonded directly to the detector pixels. The active circuitry of each pixel is a charge-sensitive preamplifier CSP (with no shaping filtering) and an output buffer which is multiplexed directly off the chip. The nine outputs from each of the four arrays are multiplexed onto a common nine-track analogue bus which is driven off chip by output buffers. The outputs of all nine pixels of the selected array are read out simultaneously allowing the analysis of the height and the shape of the pulses. The pulses are characterized by rise times of less than 60 ns and a noise (ENC)  $< 80$  electrons. The bonding process was performed at RAL by using low-temperature curing ( $<150^\circ\text{C}$ ) silver-loaded epoxy and gold stud bonding technique (Schneider *et al.*, 2015).

The output waveforms from the PIXIE ASIC are digitized and processed on-line by a 16-channel digital electronics, developed at DiFC of University of Palermo (Italy) (Abbene *et al.*, 2013a,b, 2015b; Gerardi & Abbene, 2014). The digital electronics are based on commercial digitizers (DT5724, 16-bit,  $100 \text{ MS s}^{-1}$ , CAEN SpA, Italy; <http://www.caen.it>), where an original firmware was uploaded (Abbene *et al.*, 2015b; Gerardi & Abbene, 2014). A detailed description of the digital firmware is reported in our previous works (Abbene *et al.*, 2015b; Gerardi & Abbene, 2014). The digital analysis starts with the shaping of the output waveform from the detector-ASIC by using the classical single delay line (SDL) shaping technique (Knoll, 2000). SDL shaping is obtained by subtracting from the original pulse its delayed and attenuated fraction. The typical shape of the SDL pulses is shown in Fig. 2. Generally, the SDL shaping is characterized by the following main features: (i) the time width of each SDL shaped pulse is

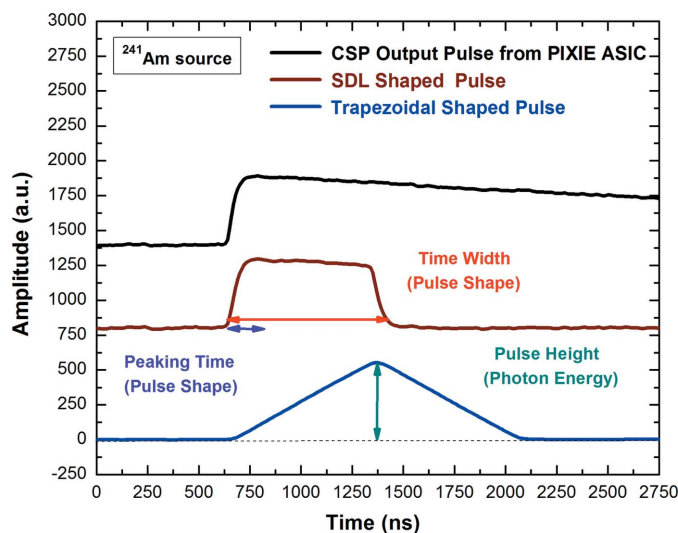


**Figure 2**  
A typical output pulse from the charge-sensitive preamplifier (CSP) of the PIXIE ASIC after digitation (black line), after SDL shaping (brown line) with a delay line of 700 ns and after trapezoidal filtering (blue line).

well defined (delay time + CSP peaking time), (ii) if the delay time is greater than the peaking time of the CSP pulse, the SDL shaping also preserves the leading edge (pulse height and peaking time) of each CSP pulse, and (iii) fine pole-zero cancellation (Knoll, 2000) is allowed by selecting the correct attenuation fraction (which is related to the decay time constant of the CSP pulses). To increase the signal-to-noise ratio (SNR) we also performed a further shaping with a trapezoidal filtering (Fig. 2). Generally, the digital electronics are able to provide different results through several working modes (Gerardi & Abbene, 2014). In this work, we used some working modes with the following results:

(i) The arrival time, the height (*i.e.* the photon energy) and time width (*i.e.* the pulse shape) of the pulses after SDL and trapezoidal shaping, presented in list-mode.

(ii) The CSP output waveform (oscilloscope mode), helpful to check the polarity of the waveform, ADC saturation and the shape of the pulses.

(iii) The SDL output waveform (oscilloscope mode), *i.e.* the pulses after SDL shaping, helpful to check the pole-zero cancellation (Knoll, 2000) and to set the amplitude threshold for pulse detection.

(iv) A sequence of time windows (termed ‘snapshots’) of the CSP output waveform; each snapshot contains a single CSP pulse, together with the related arrival time, and it is centred on each pulse peak position. This working mode is very helpful to check the shape of the CSP output pulses in temporal coincidence and also perform further off-line analysis.

### 2.3. Experimental procedures

The detectors were exposed, through the cathode side, to uncollimated X-ray and gamma-ray calibration sources ( $^{109}\text{Cd}$ : 22.1, 24.9 and 88.1 keV;  $^{241}\text{Am}$ : 59.5 and 26.3 keV;  $^{57}\text{Co}$ : 122.1 and 136.5 keV). The  $^{57}\text{Co}$  energy spectra also feature the W fluorescent lines produced in the tungsten source backing ( $K_{\alpha 1} = 59.3$  keV,  $K_{\alpha 2} = 58.0$  keV,  $K_{\beta 1} = 67.2$  keV,  $K_{\beta 3} = 66.9$  keV). The source holders shield the 14 keV gamma line of the  $^{57}\text{Co}$  source and the Np *L* X-ray lines of the  $^{241}\text{Am}$  source.

Micro-beam characterization of the detectors was carried out on the B16 test beamline at the Diamond Light Source synchrotron (Didcot, UK; [http://www.diamond.ac.uk/Beam lines/Materials/B16](http://www.diamond.ac.uk/Beam%20lines/Materials/B16)). For these measurements, the storage ring was operated at 3 GeV with a current of 250 mA. Unfocused monochromatic X-rays, below (25 keV) and above (40 keV) the *K*-shell absorption energy of the CZT material, were provided using a multi-layer monochromator. A  $10\ \mu\text{m} \times 10\ \mu\text{m}$  collimated beam was produced using a set of JJ-Slits with tungsten carbide blades. Two sets of slits were used, one at the beam entrance which was used to define the beam size and another set close to the detector to clean up any scattered X-rays. The detector system was mounted on a versatile optics table which can be moved in *X*, *Y* and *Z* with a precision of  $<1\ \mu\text{m}$ . Line scans were automated using a TTL trigger generated by the B16 control system after each  $10\ \mu\text{m}$  step

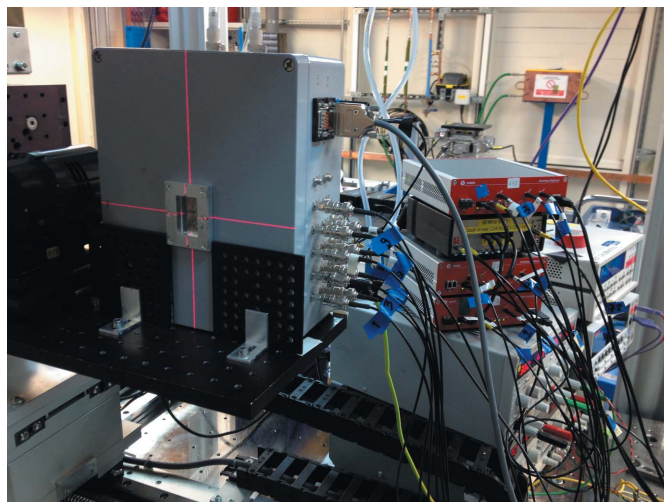


**Figure 3**

The experimental set-up used at the beamline B16 of the Diamond Light Source (UK). (Left) The box with the detectors and the PIXIE ASIC. (Right) The 16-channel digital electronics.

that began the data acquisition by the digitizers. Fig. 3 shows an overview of the experimental set-up at the beamline B16.

## 3. Measurements with uncollimated radiation sources

### 3.1. Spectroscopic performance of the detectors

In this section, we will present an overview of the spectroscopic response of the detectors to uncollimated  $^{109}\text{Cd}$ ,  $^{241}\text{Am}$  and  $^{57}\text{Co}$  sources. To optimize the energy resolution and avoid the effects of ballistic deficit (Knoll, 2000), we used a SDL shaping with a delay time of 700 ns (Fig. 2). Fig. 4 shows the measured  $^{109}\text{Cd}$  and  $^{241}\text{Am}$  spectra of pixel 9 of array 3 (pixel pitch of  $500\ \mu\text{m}$ ) for the 2 mm-thick IMEM detector. All detectors were investigated with a moderate cooling ( $T = 2^\circ\text{C}$ ) to ensure more time stability of both the detectors and the electronics, especially for long time measurements. Room-temperature measurements were also performed but showed an associated degradation of the spectroscopic performance (percentage FWHM degradation of about 8%). As shown in Fig. 4(b), the charge-sharing effects are clearly visible in the spectra: the presence of (i) tailing in the low-energy side of the main energy peak, (ii) low-energy background and (iii) fluorescent peaks (*e.g.* the Cd  $K_{\alpha 1}$  line of 23.2 keV). The energy resolution (FWHM) values for the large and small arrays of all detectors are reported in Table 1.

Generally, the two 2 mm-thick detectors (IMEM and REDLEN detectors) are characterized by similar performance. At low and medium energies (22.1 and 59.5 keV), the pixels of the large array (array 3; pixel pitch of  $500\ \mu\text{m}$ ) show similar energy resolution values for both 1 and 2 mm-thick detectors. At low energy, the energy resolution is mainly dominated by the electronic noise. Degradation of the energy resolution characterizes the pixels of the small array (array 0; pixel pitch of  $250\ \mu\text{m}$ ), especially for the 2 mm-thick detector. This, despite the better unipolar behaviour of the weighting

**Table 1**

Spectroscopic performance of the CZT pixel detectors (pixel 9) at  $T = 2^\circ\text{C}$ , after SDL (delay time of 700 ns) and trapezoidal shaping.

Bias voltages of 250 V and 1000 V were used for the 1 mm- and 2 mm-thick detectors, respectively. The Fano noise was calculated by using a Fano factor  $F = 0.1$  (Devanathan *et al.*, 2006; Kuvvetli & Budtz-Jorgensen, 2005; Owens & Peacock, 2004). No charge-sharing corrections were applied.

Detector	Array	Energy resolution FWHM at 22.1 keV (keV) Fano noise: 0.2 keV	Energy resolution FWHM at 59.5 keV (keV) Fano noise: 0.4 keV	Energy resolution FWHM at 122.1 keV (keV) Fano noise: 0.6 keV
IMEM 1 mm thick (250 V)	500 $\mu\text{m}$	1.2	1.6	3.2
	250 $\mu\text{m}$	1.3	2	2.4
IMEM 2 mm thick (1000 V)	500 $\mu\text{m}$	1.2	1.4	1.8
	250 $\mu\text{m}$	1.6	1.8	2.7
REDLEN 2 mm thick (1000 V)	500 $\mu\text{m}$	1.2	1.3	1.9
	250 $\mu\text{m}$	1.5	1.7	2.7

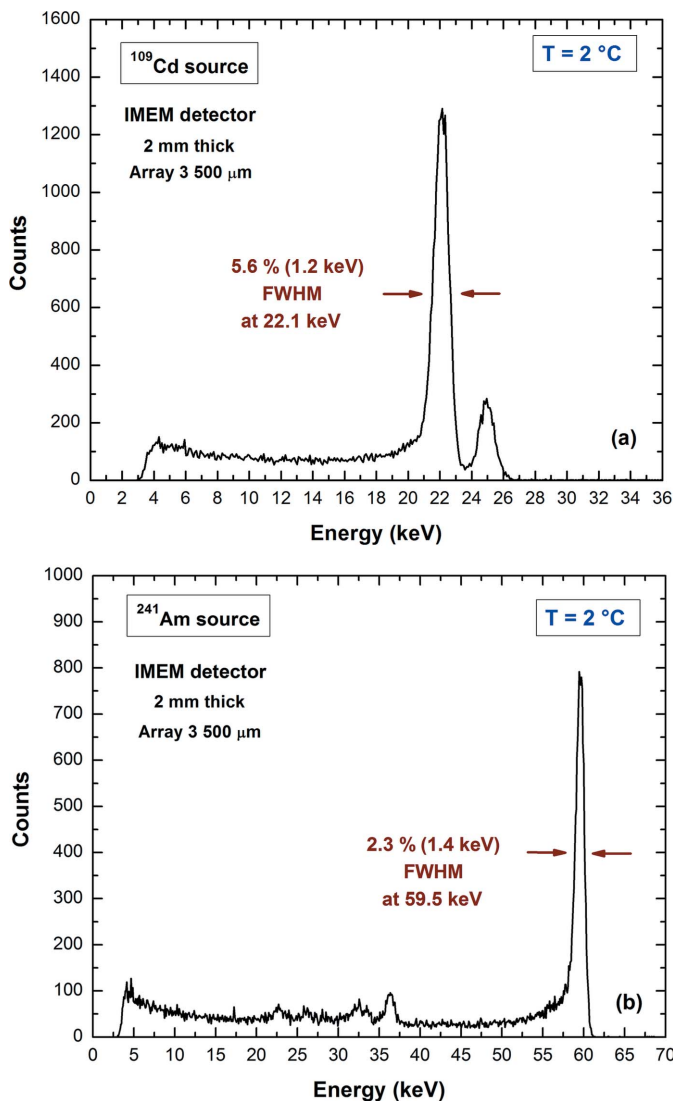


**Figure 4** Measured energy spectra of uncollimated (a)  $^{109}\text{Cd}$  and (b)  $^{241}\text{Am}$  sources of pixel 9 of the array 3 (pixel pitch of 500  $\mu\text{m}$ ) at low rate conditions ( $< 600$  counts  $\text{s}^{-1}$ ). At room temperature, we measured, for the same pixel and by using the same bias voltage, energy resolution (FWHM) values of 6% (1.3 keV) and 2.5% (1.5 keV) at 22.1 keV and 59.5 keV, respectively.

potential of the small array (small pixel effect), is due to the effects of charge sharing in the small array, which is characterized by a higher ratio between the gap area and the pixel area ( $G/A$  ratio). At high energy (122.1 keV), the signals reflect a greater contribution from the holes, and the energy spectra are characterized by the typical hole charge trapping effects, such as the degradation of energy resolution and tailing (Del Sordo *et al.*, 2009); at this energy, due to the enhanced small pixel effect (better unipolar properties, *i.e.* smaller hole contribution in the signals), the pixels of the large array of the 2 mm-thick detectors are characterized by better energy resolution than the

thin detector one, while the pixels of the small array showed a slight worsening at 122.1 keV with respect to the thin detector, due to the effects of charge sharing.

**3.2. Charge-sharing measurements**

Charge-shared events were investigated through the time coincidence analysis (TCA). In particular, we measured the events of the central pixel 5 of each array that are in temporal coincidence with the adjacent pixels, within selected coincidence time windows (CTWs). The digital electronics allow fine TCA with CTWs up to 10 ns. Table 2 summarizes the percentages of charge-shared events for the small and large arrays of all detectors. We used an energy threshold of 3 keV, representing the optimum value for no noise detection, and a CTW of 450 ns that allows a full detection of the shared events. Since the 2 mm-thick detectors (IMEM and REDLEN) have similar performance and sharing percentage values, we preferred to present in Table 2 the results for the IMEM detectors (1 mm- and 2 mm-thick detectors), at the same electric field ( $2500 \text{ V cm}^{-1}$ ) and under the optimum electric field conditions ( $2500 \text{ V cm}^{-1}$  and  $5000 \text{ V cm}^{-1}$  for the 1 mm- and 2 mm-thick detectors, respectively). We present the results at energies below ( $^{109}\text{Cd}$ ) and above ( $^{241}\text{Am}$ ) the  $K$ -shell absorption energy of the CZT material.

Fig. 5(a) shows the number of shared events of the central pixel with the eight adjacent pixels at different CTWs (2 mm-thick REDLEN detector). Almost all shared events ( $> 94\%$ ) are detected within a CTW of 50 ns and the saturation of the curves clearly shows the full detection of the shared events within the investigated CTW range. Due to the higher  $G/A$  ratio, the small array (array 0) is characterized by more charge-sharing events; moreover, the difference in charge sharing between the energies below ( $^{109}\text{Cd}$ ) and above ( $^{241}\text{Am}$ ) the  $K$ -shell absorption energy of the CZT material points out the critical role of the X-ray fluorescence. Fluorescent X-rays broaden the initial electron cloud and can create cross-talk events in neighbouring pixels (side and back escape events). The improvements in the energy spectrum after CSD

**Table 2**

Charge-sharing percentages among the central pixel (pixel 5) and the eight adjacent pixels of the CZT pixel detectors (IMEM detectors) at  $T = 2^\circ\text{C}$ .

The shared events were detected within a coincidence time window (CTW) of 450 ns and with an energy threshold of 3 keV. The 2 mm-thick detectors (IMEM and REDLEN detectors) are characterized by similar sharing percentages.

Detector	Array	Sharing percentage at 22.1 keV (%)	Sharing percentage at 59.5 keV (%)
IMEM	500 $\mu\text{m}$	27	49
1 mm thick (2500 V $\text{cm}^{-1}$ )	250 $\mu\text{m}$	48	76
IMEM	500 $\mu\text{m}$	43	66
2 mm thick (2500 V $\text{cm}^{-1}$ )	250 $\mu\text{m}$	58	86
IMEM	500 $\mu\text{m}$	36	59
2 mm thick (5000 V $\text{cm}^{-1}$ )	250 $\mu\text{m}$	52	81

are shown in Fig. 5(b). In particular, three different spectra are presented for the central pixel: (i) the raw spectrum after energy calibration (black line), (ii) the spectrum of the coincidence events with all eight adjacent pixels (red line) and (iii) the spectrum after CSD (blue line). The strong reduction of the shared events in the spectrum after CSD is clearly visible. The low-energy side of the raw spectrum perfectly coincides with the spectrum of the coincidence events and the fluorescent X-rays are deleted after CSD.

Some escape peaks are present in the  $^{241}\text{Am}$  spectra even after CSD, due to the back escape events (e.g. from the cathode side) and fluorescence events absorbed beyond the adjacent pixels (i.e. absorbed below the guard-ring electrode). With the energy threshold (3 keV) used in the sharing detection, no improvements in the energy resolution of the main peaks were obtained after CSD.

To recover the shared events, rejected after CSD, we applied the CSA technique. The energy ( $E_{\text{CSA}}$ ) recovered after CSA is obtained by summing the energies of the coincidence events between two adjacent pixels (multiplicity  $m = 2$ ). The multiplicity  $m$  is defined as the number of pixels detecting an event within the selected CTW, with an energy greater than the energy threshold of 3 keV. Each of the detectors tested demonstrated an increase in FWHM in the energy spectra after CSA. Moreover, a reduction in the position of the peak centroid was also observed, related to charge losses occurring in the inter-pixel gap. Fig. 6 shows the energy spectra after CSA, related to the coincidence events between two adjacent pixels (pixels 5 and 8 of the 500  $\mu\text{m}$  array), for the 1 mm- and 2 mm-thick detectors. At energy (22.1 keV) below the  $K$ -shell absorption energy of the CZT material energy, all detectors and arrays showed a charge loss of about 2 keV; at higher energy (60 keV), where charge sharing is increased by X-ray fluorescence, charge losses are more severe (4 keV). Moreover, these losses are enhanced for the pixels of the small array (6 keV). We also observed that the charge loss depends on the bias voltage; e.g. the pixels of the large arrays of the 2 mm-thick detectors are characterized

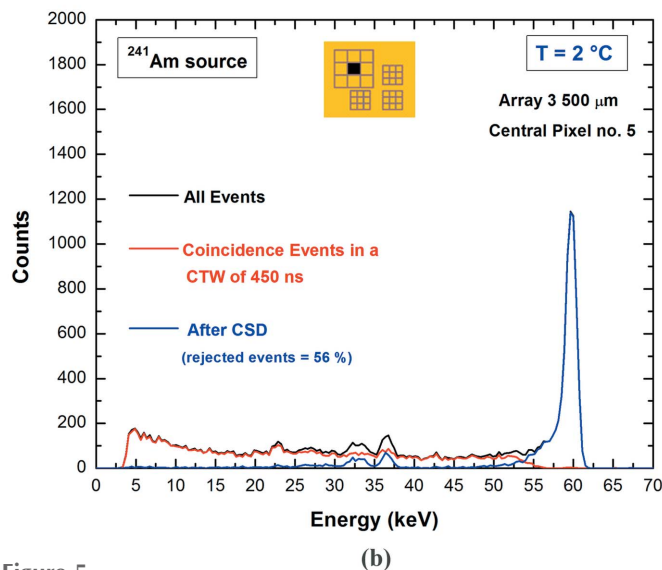
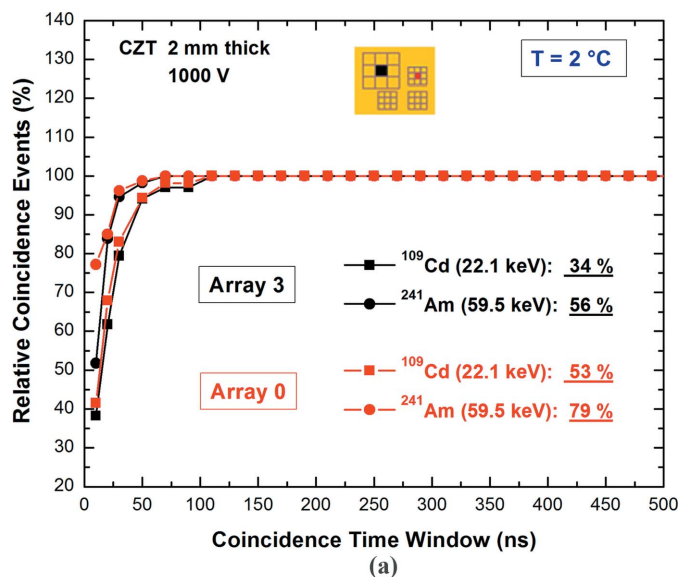


**Figure 5**

(a) Relative coincidence events (percentage) of the central pixel 5 of the 2 mm-thick REDLEN detector, for the array 3 and array 0, with the eight adjacent pixels at different CTWs and energies ( $^{109}\text{Cd}$ ,  $^{241}\text{Am}$ ). The absolute percentage values of the coincidence events (within a CTW of 450 ns) are also shown (energy threshold of 3 keV). (b) The raw  $^{241}\text{Am}$  spectrum of the central pixel (black line), the spectrum of the coincidence events with all eight adjacent pixels (red line) and after charge-sharing discrimination (CSD) (blue line).

by a charge loss of 7 keV at 500 V (4 keV at 1000 V). This last result strengthens the idea that charge losses after CSA are mainly related to the electron trapping in the inter-pixel region due to the presence of lower electric field.

Fig. 7 also shows the energy  $E_{\text{CSA}}$  after CSA versus the charge-sharing ratio  $R$ , between the two pixels. The charge-sharing ratio  $R$  is typically used to provide information about the interaction position of the shared events and is generally calculated from the ratio between the energy of the pixel events, as follows:  $R = (\text{pixel 5} - \text{pixel 8}) / (\text{pixel 5} + \text{pixel 8})$ . The curvature shows that the shared events do not have 100% efficient charge collection and that charge losses are more severe for those events for which  $R$  is zero, theoretically

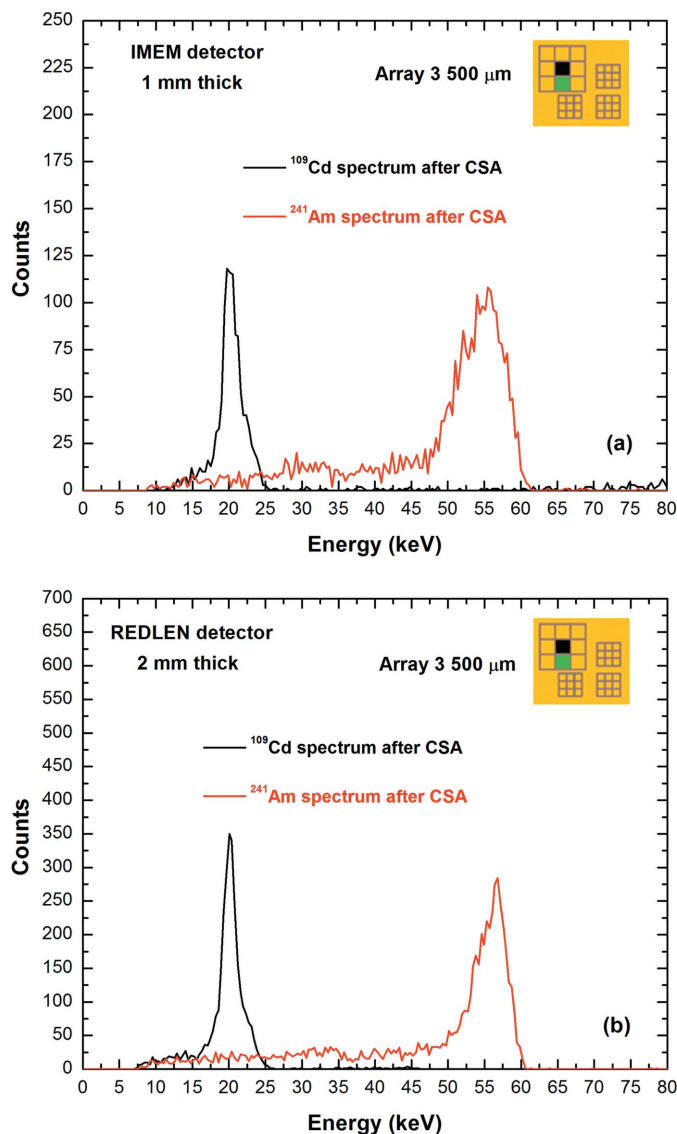


**Figure 6** The energy spectra of the coincidence events, between the pixels 5 and 8, after charge-sharing addition (CSA) for the (a) 1 mm-thick and (b) 2 mm-thick detectors. Both detectors clearly highlight the presence of charge losses near the inter-pixel gap.

related to events stopped at the centre of the inter-pixel gap. The two kinks at  $R = \pm 0.22$  are due to the escape of the fluorescent X-rays of the CZT material. In the distribution shown in Fig. 7, the majority of interactions have combined energies of no more than 60 keV. This demonstrates that the majority of events are true charge-shared events. False shared events can be created by photons interacting simultaneously on the neighbouring pixels or by induced-charge pulses with positive polarity (Bolotnikov *et al.*, 2016; Kim *et al.*, 2011; Zhu *et al.*, 2011).

#### 4. Microscale line scanning with collimated synchrotron X-rays

Collimated synchrotron X-rays, at the B16 beamline of Diamond Light Source, were used to investigate charge-

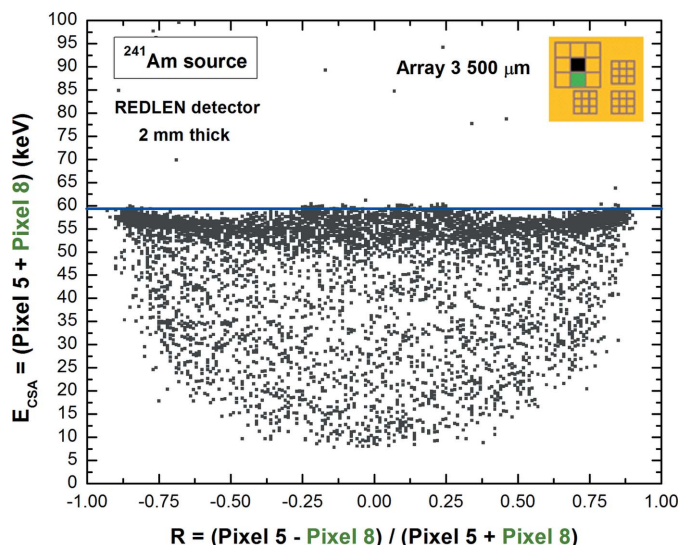


**Figure 7** Two-dimensional scatter plot of the energy  $E_{\text{CSA}}$  of the coincidence events ( $m = 2$ ), between the pixels 5 and 8, after CSA. The energy  $E_{\text{CSA}}$  is plotted *versus* the charge-sharing ratio  $R$ , which gives information about the interaction position of the events. The shift of the track to lower energies than 59.5 keV (blue line) is due to charge losses near the inter-pixel region. The two kinks at  $R = \pm 0.22$  are due to the escape of the fluorescent X-rays of the CZT material (*e.g.* the Cd  $K_{\alpha 1}$  fluorescent line is characterized by an energy of 23.2 keV).

sharing and charge-loss effects on a sub-pixel level. The results of a microscale line scanning between the centres of two adjacent pixels (pixels 5 and 8) are presented. We used collimated ( $10 \mu\text{m} \times 10 \mu\text{m}$ ) synchrotron X-ray beams with energies below (25 keV) and above (40 keV) the  $K$ -shell absorption energy of CZT material, with position steps of  $10 \mu\text{m}$ . During the line scanning between the two pixels, we acquired, at each beam position, the data from all nine pixels of the investigated array. Fig. 8 shows an overview of the variation of the photopeak centroid of the main peak (25 keV) and the multiplicity  $m$  with changing beam position for the 1 mm- and 2 mm-thick detectors.

Centroid variations are observed in a region of  $100 \mu\text{m}$  that is centred on the middle of the inter-pixel region. For both of the detectors tested, coincidence events ( $m > 1$ ) were only detected at beam positions within  $100 \mu\text{m}$  of the centre of the inter-pixel region. At the centre of the inter-pixel gap, 100% of events were shared between the two pixels.

At 40 keV (Fig. 9), coincidence events were detected in a wider region, even for beam positions near the centre of the pixels. This is due to the propagation of fluorescent X-rays that increases the initial charge cloud and creates cross-talk events. The attenuation lengths of the Cd  $K_{\alpha}$  and Cd  $K_{\beta}$  X-rays are  $116 \mu\text{m}$  and  $161 \mu\text{m}$ , respectively (Abbene *et al.*, 2018; Allwork *et al.*, 2012). At the centre of the inter-pixel gap, 96% of the events are shared between pixels 5 and 8 ( $m = 2$ ), while 4% with other pixels ( $m > 2$ ). As shown in the literature (Bolotnikov *et al.*, 2016; Montémont *et al.*, 2014), the energy and the multiplicity of the coincidence events can be helpful to measure the locations of interaction points with sub-pixel spatial resolution.

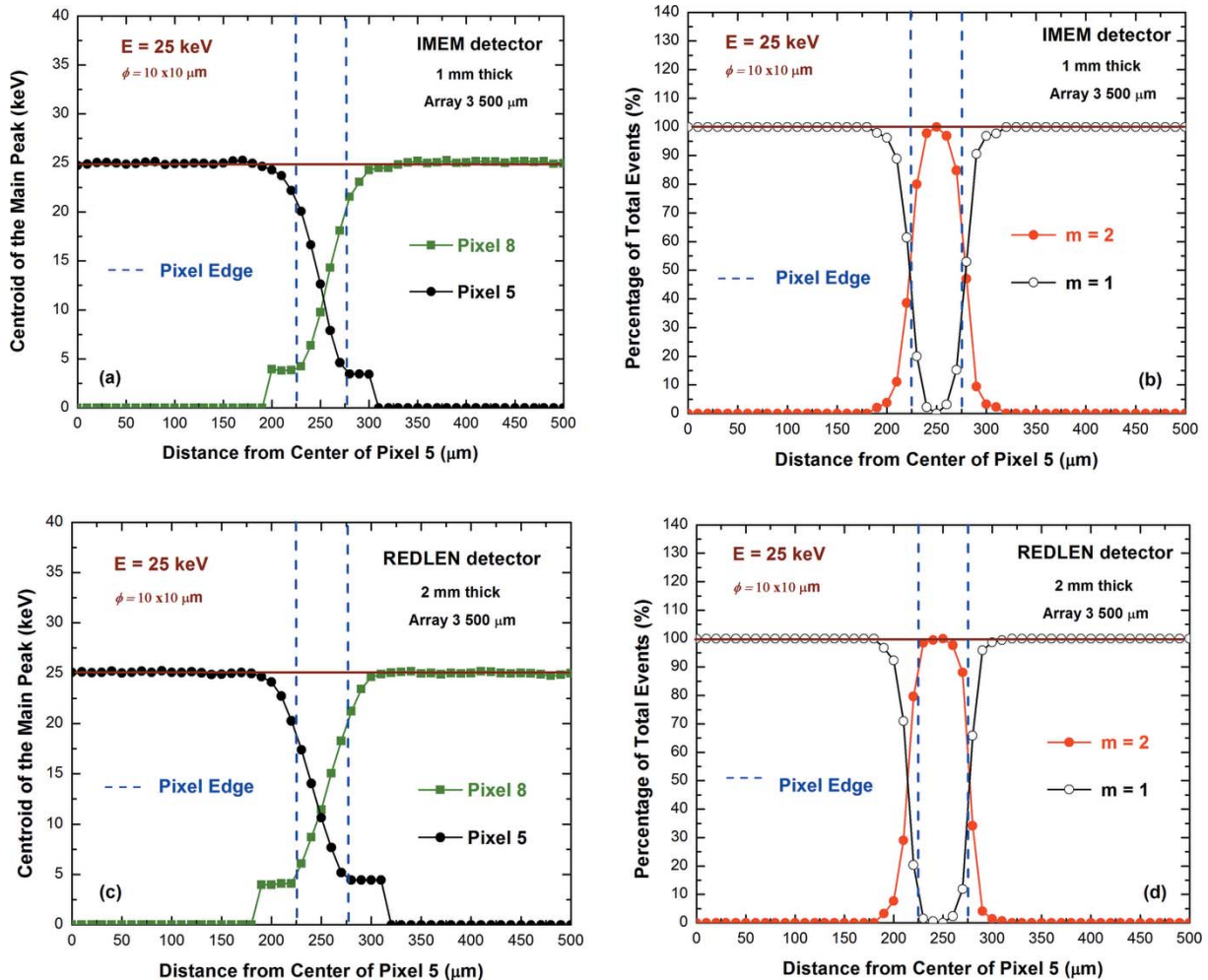


**Figure 8** Results of a microscale line scanning (position steps of 10  $\mu\text{m}$ ) between the centres of two adjacent pixels (pixels No. 5 and No. 8) at energy below (25 keV) the  $K$ -shell absorption energy of CZT material. Photopeak centroids and multiplicity  $m$  for the (a), (b) 1 mm-thick and (c), (d) 2 mm-thick detectors. (a) The jump discontinuities present in the curves for peak centroid values around 4 keV are due to the non-zero energy threshold (3 keV).

The presence of charge losses after CSA was also confirmed with collimated beams ( $10\ \mu\text{m} \times 10\ \mu\text{m}$ ). The energy spectra after CSA for a beam position at the centre of the inter-pixel gap are shown in Fig. 10. We measured the CSA spectra, between pixels 5 and 8, for the large and the small arrays of the 2 mm-thick REDLEN detector. The main peaks are both widened and shifted to lower energies confirming the presence of charge losses at the inter-pixel gap. The presence of charge losses at 25 keV allows us to exclude the non-zero energy threshold of the electronics as the possible cause of charge losses.

We also presented, at the same beam position, the two-dimensional scatter plot of the energy  $E_{\text{CSA}}$  after CSA versus the charge-sharing ratio  $R$  (Fig. 11). The spreading of the ratio  $R$  at this collimated beam position is also shown. The  $R$  distribution at 40 keV (Fig. 11d) clearly shows the presence of secondary peaks, due to the presence of fluorescent X-rays. Fig. 12 shows the relationship between the charge-sharing ratio  $R$  and the real interaction position within the inter-pixel gap. To a first-order approximation, a linear function can be used to define the position of the beams in the inter-pixel gap.

### 5. Charge-loss correction at the inter-pixel gap

In this section, we will present an original technique able to correct the charge losses after CSA. The technique exploits the strong relation between the energy  $E_{\text{CSA}}$  after CSA and the charge-sharing ratio  $R$  (Figs. 7 and 11). The relation between the energy  $E_{\text{CSA}}$  and  $R$  was modelled through the following equation:

$$E_{\text{CSA}}(R) = E - \Delta E_{\text{CSA}}(0) (1 - R^2), \quad (1)$$

where  $E$  is the true photon energy and  $\Delta E_{\text{CSA}}(0) = E - E_{\text{CSA}}(0)$  is the energy lost at the centre of the inter-pixel gap ( $R = 0$ ). Fig. 13(a) shows the energy  $E_{\text{CSA}}$  at different  $R$  values. Each  $R$  value corresponds to a real beam position ( $10\ \mu\text{m} \times 10\ \mu\text{m}$ ) within the inter-pixel gap with a position step of  $10\ \mu\text{m}$ . The energy  $E_{\text{CSA}}$  was calculated as the centroid of the main photopeak of each spectrum obtained after CSA. The curves, obtained at three different energies, are well modelled by equation (1). Moreover, it is interesting to note the linear behaviour of the energy lost  $\Delta E_{\text{CSA}}(0)$  with the true energy  $E$ , as shown in Fig. 13(b):

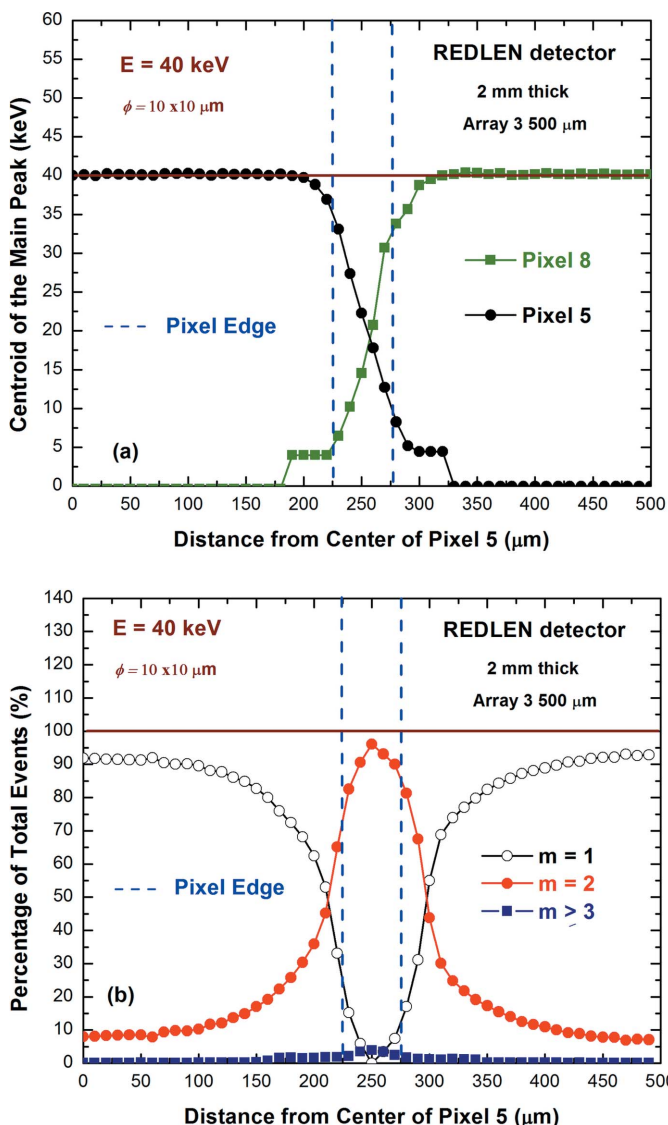


**Figure 9** Results of a microscale line scanning (position steps of 10  $\mu\text{m}$ ) between the centres of two adjacent pixels (pixels No. 5 and No. 8) at energy above (40 keV) the  $K$ -shell absorption energy of CZT material. (a) Photopeak centroids and (b) multiplicity  $m$  for the 2 mm-thick detector were calculated. At 40 keV, even for beam positions near the centre of the pixels, the multiplicity is  $m \geq 1$ , due to the presence of fluorescent X-rays. (a) The jump discontinuities present in the curves for peak centroid values around 4 keV are due to the non-zero energy threshold (3 keV).

$$\Delta E_{\text{CSA}}(0) = k_1 + k_2 E, \quad (2)$$

where  $k_1$  and  $k_2$  are the slope and the  $y$ -intercept of the linear function. Combining (1) and (2) yields

$$E_{\text{cor}} = E = \left[ \frac{E_{\text{CSA}}(R) + k_1(1 - R^2)}{1 - k_2(1 - R^2)} \right]. \quad (3)$$

By using (3) it is possible to correct the charge losses after CSA through the measurement of the bi-parametric distribution  $E_{\text{CSA}} - R$  and the estimation of the constants  $k_1$  and  $k_2$ , which can be obtained by a preliminary calibration procedure [equations (1) and (2)]. We stress that this correction does not depend on the photon energy but it is related to the physical

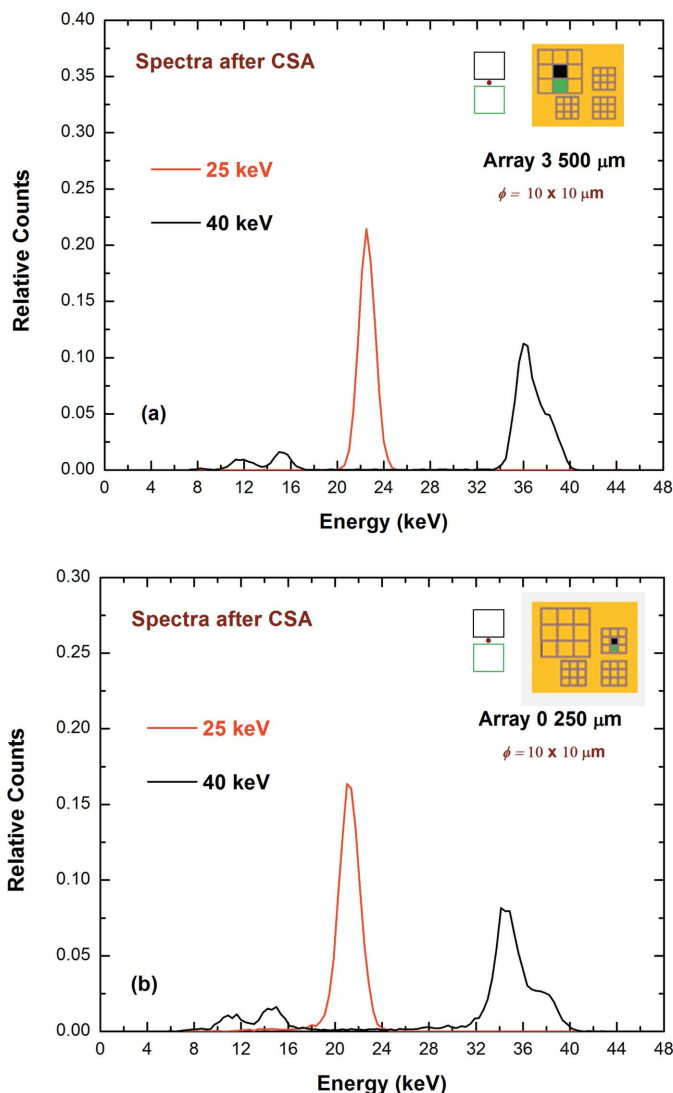


**Figure 10** The energy spectra after CSA with the collimated synchrotron X-ray beams positioned at the centre of the inter-pixel gap between pixels 5 and 8 of (a) the 500  $\mu\text{m}$  and (b) 250  $\mu\text{m}$  arrays of the 2 mm-thick REDLEN detector. The photopeaks are both widened and shifted to lower energies (energy shifts  $> 10\%$ ), confirming the presence of charge losses at the inter-pixel gap.

and geometrical characteristics of the inter-pixel gap, in particular the ratio between the gap area and the pixel area. Indeed, we obtained, for the pixels of a fixed array the same values of  $k_1$  and  $k_2$  for all detectors (500  $\mu\text{m}$  array:  $k_1 = 0.009 \text{ keV}$  and  $k_2 = 0.10 \text{ keV}^{-1}$ ; 250  $\mu\text{m}$  array:  $k_1 = 0.015 \text{ keV}$  and  $k_2 = 0.14 \text{ keV}^{-1}$ ). Fig. 14 clearly shows the recovery of the charge losses after CSA and improvements in the energy resolution (collimated beam at the centre of the inter-pixel gap).

We also applied this technique for uncollimated irradiation. Fig. 15 shows the good agreement between the  $E_{\text{CSA}} - R$  points with equation (1) and the energy spectra after CSA (black line) and after correction with equation (3) (red line) to the uncollimated  $^{109}\text{Cd}$  source. The  $^{241}\text{Am}$  spectra are also presented for the small and the large arrays (Fig. 16).

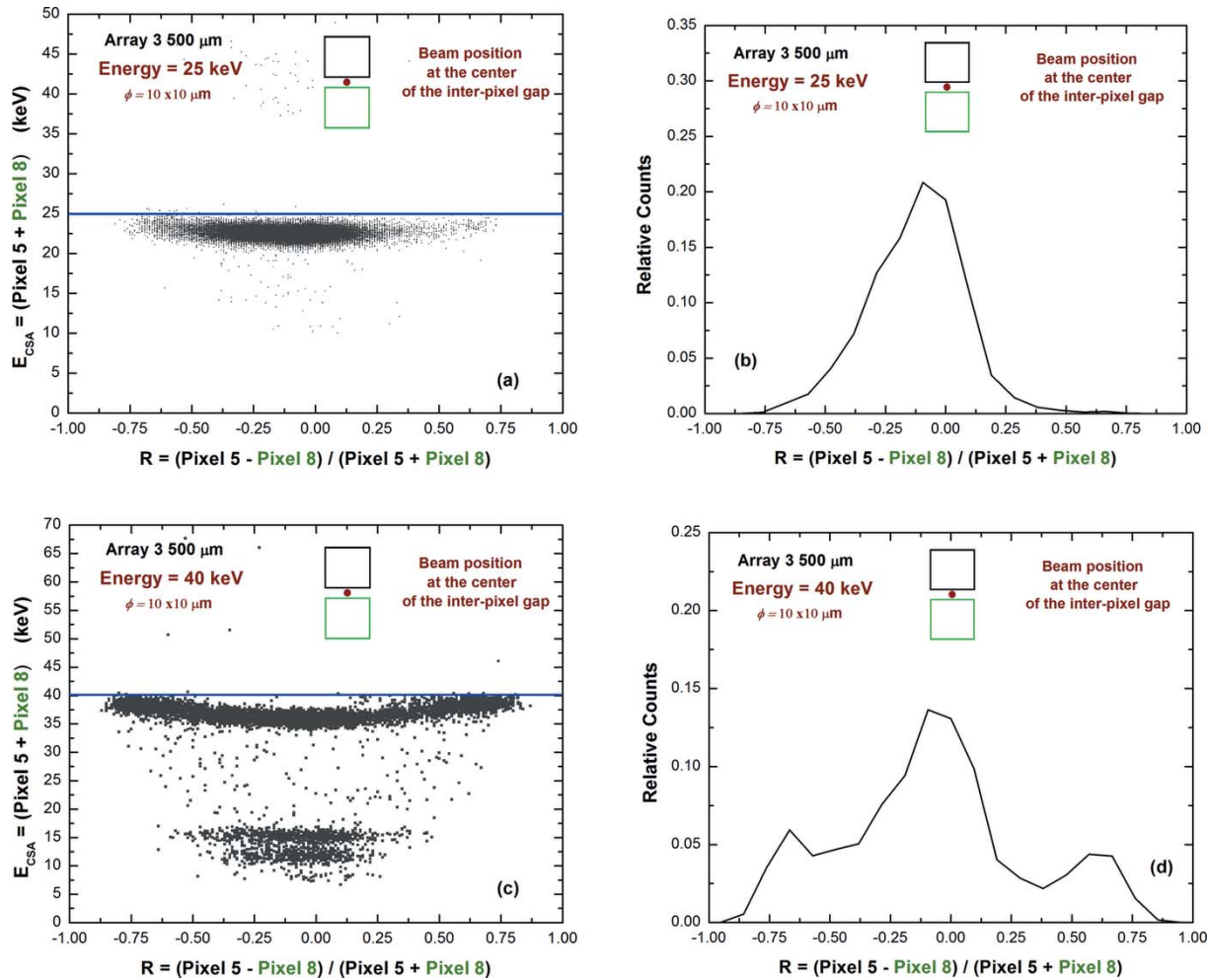


**Figure 11** Two-dimensional scatter plots of the energy  $E_{CSA}$  after CSA versus the sharing ratio  $R$ , at (a) 25 keV and (c) 40 keV. The  $R$  distributions are also shown at (b) 25 keV and (d) 40 keV. These results are related to the 2 mm-thick REDLEN detector.

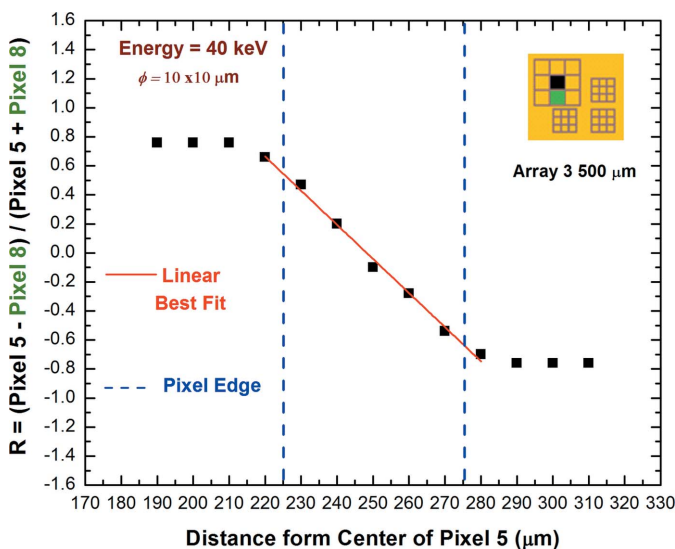


**Figure 12** The charge-sharing ratio  $R$  versus the real beam position at the inter-pixel gap between pixels 5 and 8 of the 2 mm-thick REDLEN detector. To a first-order approximation, a linear function can be used to define the position of the beams in the inter-pixel gap. Similar results were obtained for all detectors.

### 6. Analysis of negative pulses for charge-loss correction

Measurements at the energies of the  $^{57}\text{Co}$  source highlighted the presence of pulses with opposite polarity (negative polarity), with respect to standard pulses (positive polarity), in the output CSP waveforms of all detectors. Moreover, as shown in Fig. 17, these events were always detected in temporal coincidence with positive pulses of adjacent pixels. In particular, Fig. 17 shows the temporal coincidence of a positive pulse of the central pixel with the negative pulses of three adjacent pixels. The appearance of negative pulses in CZT pixel detectors was already predicted and observed in the past (Budtz-Jørgensen & Kuvvetli, 2017; Eskin *et al.*, 1999; Hong *et al.*, 2006; Zhu *et al.*, 2011). The negative pulses are induced-charge pulses produced by non-collecting pixels and they are mainly related to photon interactions near the pixel boundary and at interaction depths close to the pixel plane (*i.e.* the pixelated anode). As is well known, the output detector pulses are typically classified as collected- and induced-charge pulses (or transient pulses). The collected-charge pulses are generated by the charge carriers actually collected by a pixel, while the induced-charge pulses are

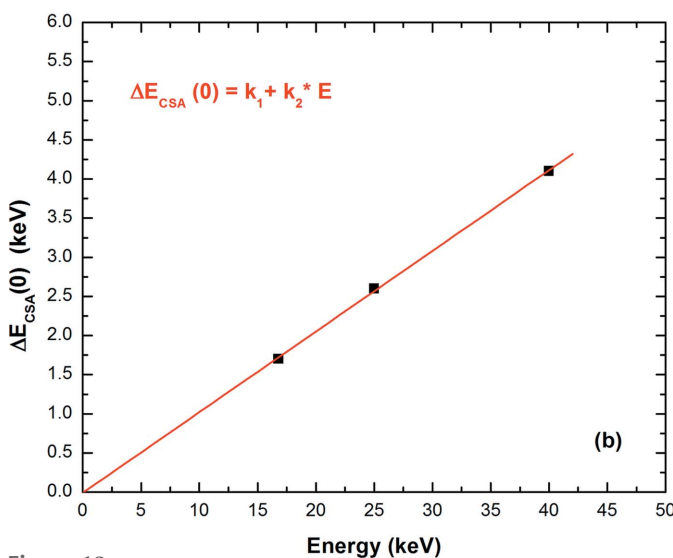
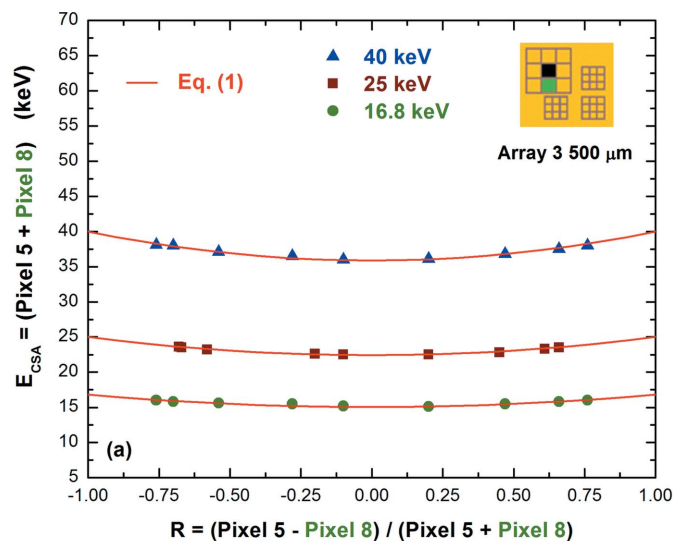


**Figure 13** (a) The energy  $E_{CSA}$  after CSA versus the charge-sharing ratio  $R$  for the 2 mm-thick REDLEN detector. Each  $R$  value corresponds to a real beam position ( $10\ \mu\text{m} \times 10\ \mu\text{m}$ ) within the inter-pixel gap with a position step of  $10\ \mu\text{m}$ . The curves are well fitted by equation (1). (b) The linear behaviour of the charge loss  $\Delta E_{CSA}(0)$  with the true photon energy  $E$ .

generated by the induced charge, collected by another pixel. The induced-charge pulses are fast pulses that in the absence of charge trapping will drop quickly to a zero value. For interactions just outside the pixel boundary and at depths near the pixelated anode, the collecting pixel will give a positive collected-charge pulse, which will be in temporal coincidence with a negative induced-charge pulse generated by the adjacent pixel. The monotonic weighting potential of the collecting pixel will give a positive pulse, even if characterized by charge losses; this is due to the effects of hole trapping that is more severe for interaction depths near the pixel (Barrett *et al.* 1995; Eskin *et al.*, 1999; Mardor *et al.*, 2001; He, 2001); whereas the adjacent pixel (*i.e.* the non-collecting pixel), due to the non-monotonic behaviour of the weighting potential (Abbene *et al.*, 2018; Eskin *et al.*, 1999) and to the hole trapping, can give a fast transient pulse with negative polarity.

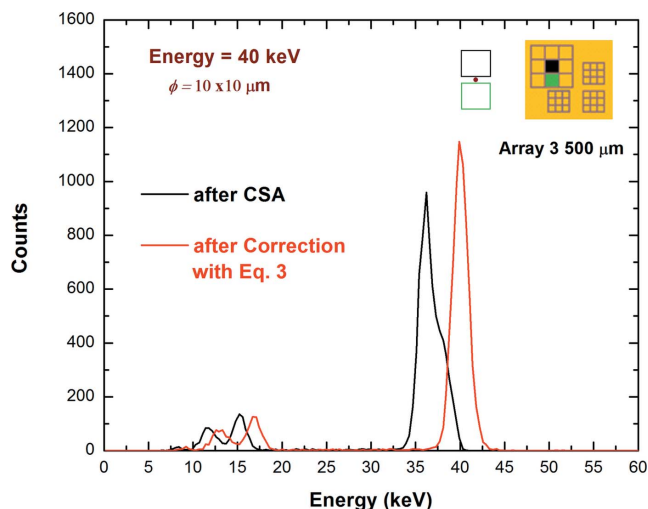


**Figure 14** The energy spectra for a collimated synchrotron beam (40 keV) at the centre of the inter-pixel gap between pixels 5 and 8 for the 2 mm-thick REDLEN detector. The spectrum after CSA (black line) and after the proposed correction technique (red line) with equation (3).

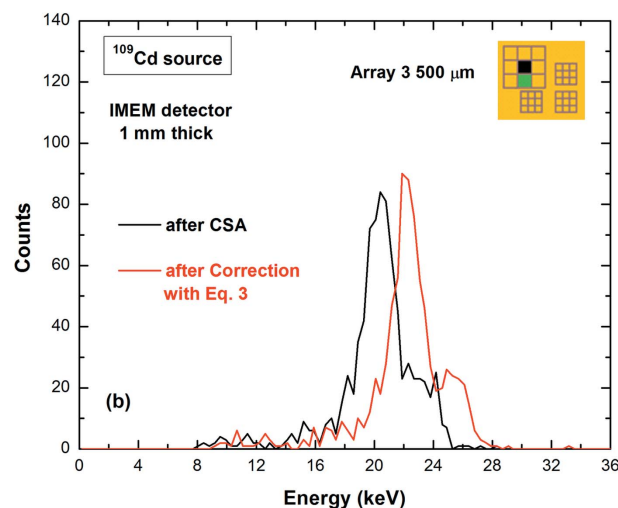
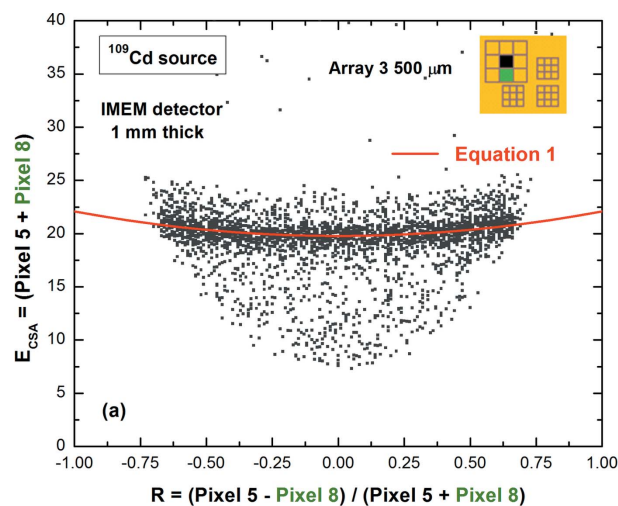


**Figure 15** (a) The energy  $E_{CSA}$  after CSA versus the charge-sharing ratio  $R$  for uncollimated irradiation, well fitted by equation (1). (b) The energy spectra after CSA (black line) and after the proposed correction technique (red line) with equation (3).

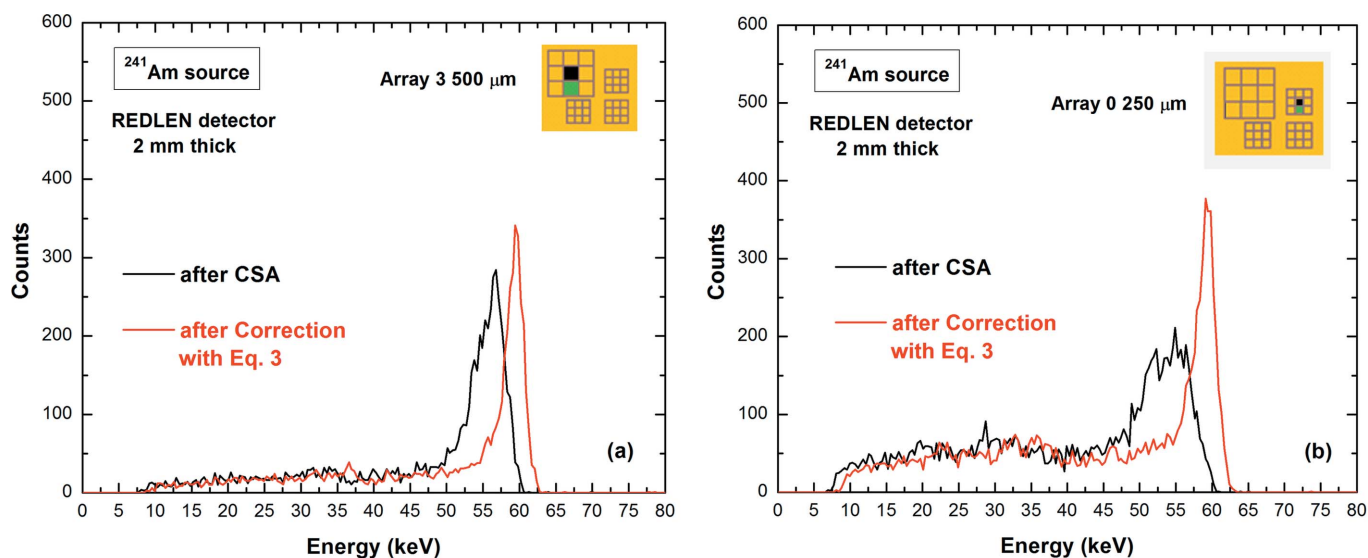


**Figure 16**  
The energy spectra after CSA (black line) and after the proposed correction technique (red line) with equation (3). The results for the pixels of (a) array 3 and (b) array 0 of the 2 mm-thick REDLEN detector.

Two main features characterize the negative pulses; first, they are characterized by a different shape than the positive ones, as shown in Fig. 17; second, they are in temporal coincidence with positive pulses characterized by charge losses due to hole trapping.

Concerning the first feature, the different shape (*i.e.* the different decay time) of the negative pulses can produce distortions after the shaping operation, as shown in Fig. 18. By selecting the correct value of the decay time, the positive SDL shaped pulse is characterized by no undershoot at the baseline, confirming a proper application of the pole-zero cancellation technique; whereas the negative pulse after the SDL shaping, applied with the same decay time constant of the positive pulses, presents a positive overshoot at the baseline. This positive overshoot can be detected as a positive event that is in temporal coincidence with another positive pulse of an adjacent pixel, *i.e.* producing as a false detection of a shared event. The detection of these false shared events will distort the statistics of the shared events and the application of CSA. Moreover, the presence of these positive overshoots can distort the correct estimation of the baseline, especially at high rates.

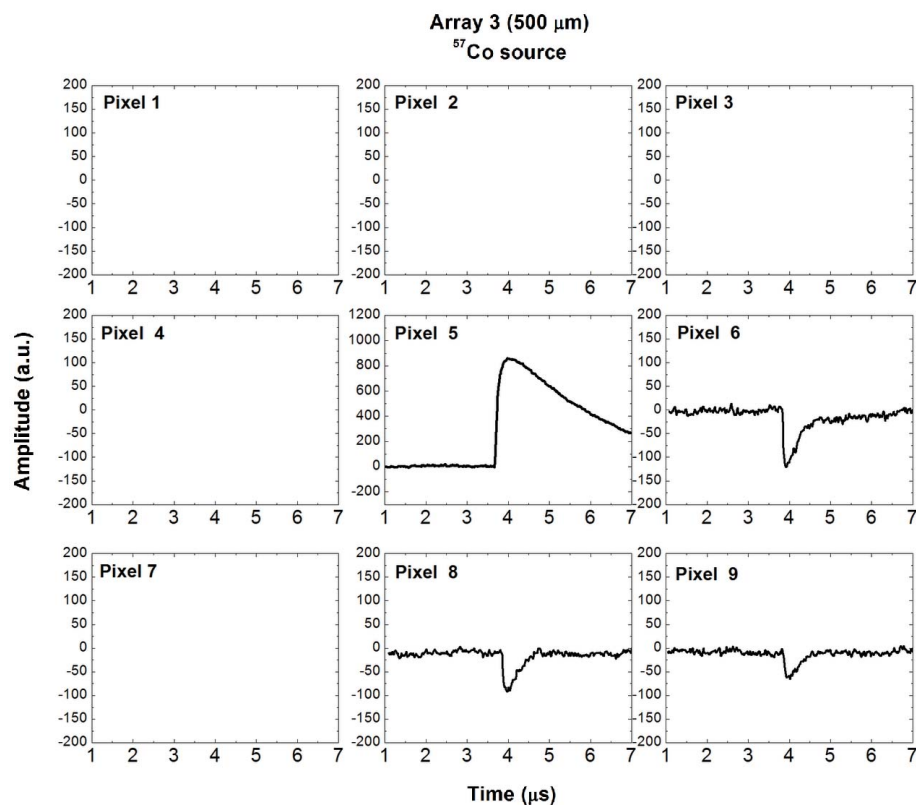


**Figure 17**  
Temporal coincidence involving a positive pulse of the central pixel with negative pulses ( $^{57}\text{Co}$  source) of the adjacent pixels (2 mm-thick REDLEN detector). The pulses are in temporal coincidence within a coincidence time window of 10 ns.

The second feature of the negative pulses was used to try to correct the positive pulses that suffer from incomplete charge collection. The coincidence measurements showed that the positive pulses of the central pixel of the large array are in temporal coincidence with the negative pulses of the eight adjacent pixels with percentages of 5% and 16% for the 2 mm- and 1 mm-thick detectors, respectively (energy threshold of 7 keV). In particular, Fig. 19(a) shows

The second feature of the negative pulses was used to try to correct the positive pulses that suffer from incomplete charge collection. The coincidence measurements showed that the positive pulses of the central pixel of the large array are in temporal coincidence with the negative pulses of the eight adjacent pixels with percentages of 5% and 16% for the 2 mm- and 1 mm-thick detectors, respectively (energy threshold of 7 keV). In particular, Fig. 19(a) shows

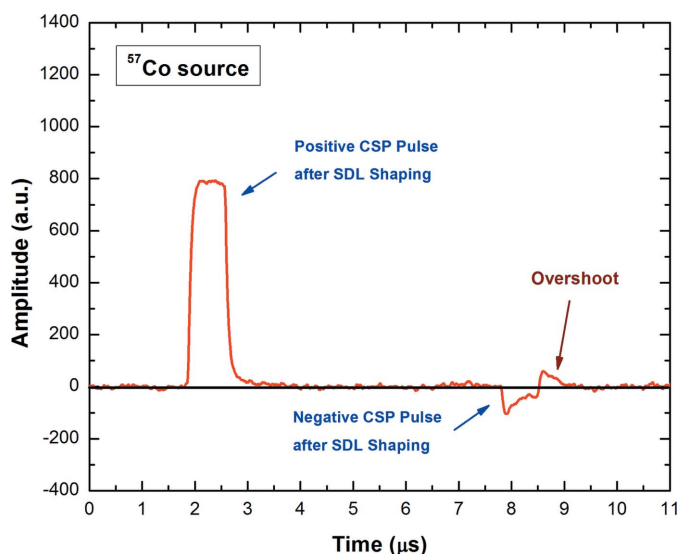


**Figure 18** Positive and negative CSP pulses after SDL shaping (2 mm-thick REDLEN detector). Due to the different decay time of the negative pulses if compared with the positive pulses, the SDL shaping will produce positive overshoots that can be detected as false positive events. Since these events are in temporal coincidence with other positive pulses, false shared events can be detected.

three different energy spectra of the positive events of the central pixel: the raw spectrum of the central pixel 5 (black line), the spectrum of the coincidence events with the negative pulses of the adjacent pixels (red line) and after charge-sharing discrimination (CSD) (blue line). It is clearly visible as the positive pulses, in temporal coincidence with the negative pulses, are positioned in the tailing of the 122 keV photopeak, confirming that they suffer from charge losses. This result is also confirmed by the high values of the time widths of the coincidence positive pulses (SDL shaped pulses), reflecting the hole trapping influence.

An interesting result was obtained by summing the energy of the coincidence positive pulses with the absolute value of the energy of the negative pulses (events with multiplicity  $m = 2$ ). After the negative induced addition (NIA), the charge losses were recovered, as shown in Fig. 20, for both the 1 mm- and 2 mm-thick detectors. It means that the double coincidences between the positive and negative pulses occur at interaction positions where the charge deficit of the positive pulse, due to the hole trapping, is the same of the absolute height of the negative pulse. Further measurements at higher energies could be helpful to understand these last results.

## 7. Conclusions

Charge-sharing investigations were performed in CZT pixel detectors, fabricated by different manufacturers (Redlen Technologies and IMEM-CNR). The detectors with sub-millimetre pixels (pixel pitches of 500 and 250  $\mu\text{m}$ ) allow high-bias voltage operation (5000  $\text{V cm}^{-1}$ ) and good energy resolution (3% and 2% FWHM at 60 and 122 keV, respectively) with a moderate cooling ( $T = 2^\circ\text{C}$ ). Charge losses after the

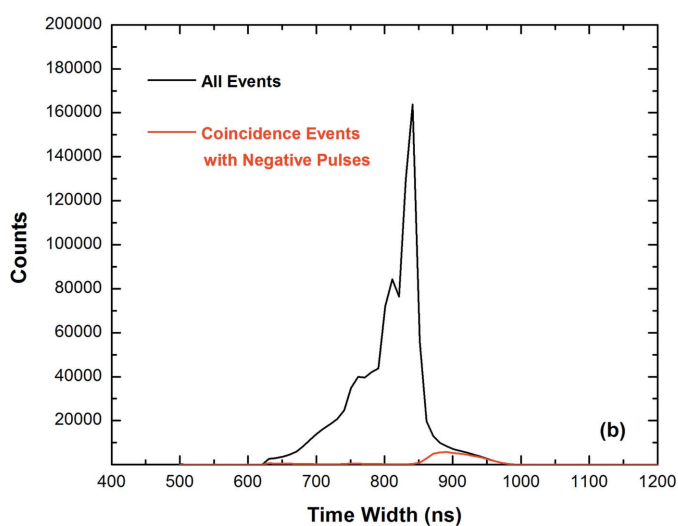
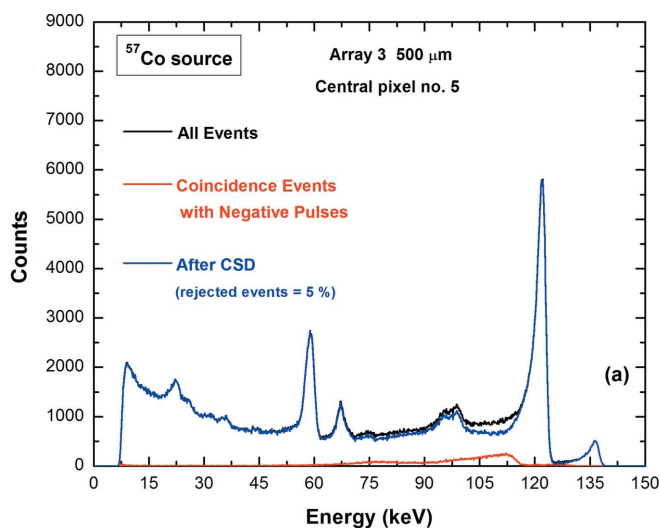


**Figure 19** (a) The raw spectrum of the central pixel 5 (black line), the spectrum of the coincidence events with the negative pulses of the eight adjacent pixels (red line) and after charge-sharing discrimination (CSD) (blue line) for the 2 mm-thick REDLEN detector. (b) The time width distribution (with time bin widths of 10 ns) of all positive pulses of the central pixel 5 (black line) and of the coincidence positive pulses (red line). An energy threshold of 7 keV was used.

application of CSA were observed in all detectors with both collimated and uncollimated X-ray beams, in particular:

(i) at energies (22.1 keV; uncollimated X-ray source) below the *K*-shell absorption energy of the CZT material, all detectors and arrays showed the same charge losses of about 2 keV;

(ii) at higher energies (60 keV; uncollimated X-ray source), where charge sharing is increased by X-ray fluorescence, charge losses are more severe (4 keV); moreover, these losses are enhanced for the pixels of the small array (6 keV), *i.e.* by increasing the ratio between the gap area and the pixel area;

(iii) charge losses depend on the bias voltage: *e.g.* the pixels of the large arrays of the 2 mm-thick detectors are characterized by a charge loss of 7 keV at 500 V and 4 keV at 1000 V (60 keV; uncollimated X-ray source);

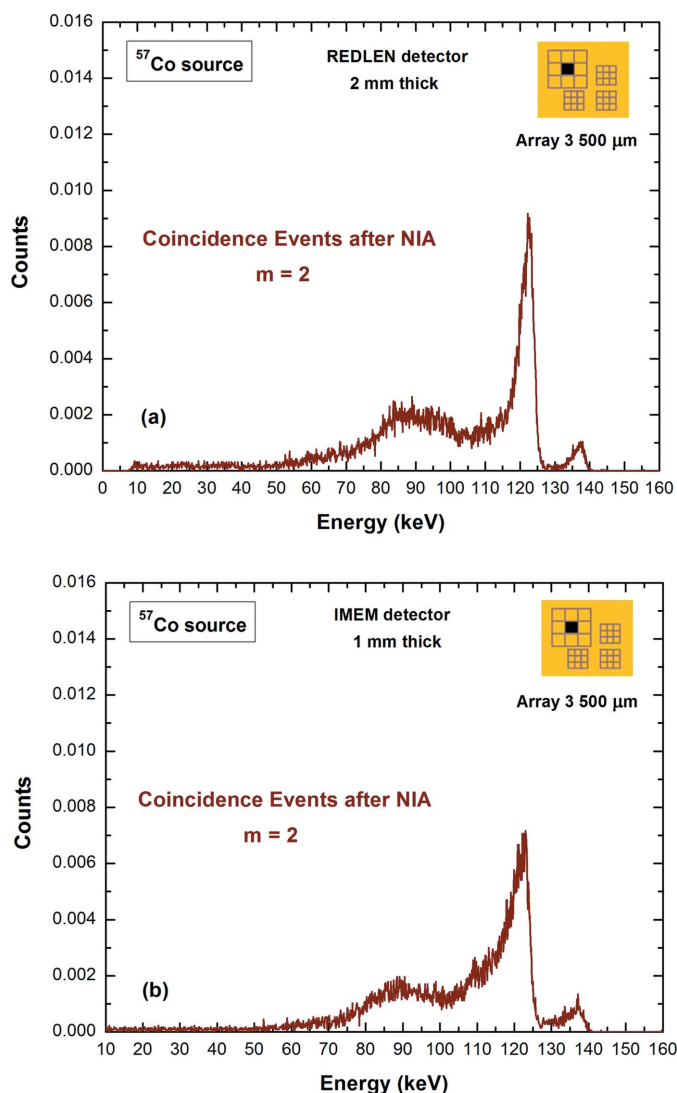


Figure 20

The energy spectra of the central pixel of the (a) 2 mm-thick REDLEN and (b) 1 mm-thick IMEM detectors after negative induced addition (NIA). The spectra are obtained by summing the energies of the positive pulses of the central pixel with the energies (absolute value) of the other negative pulses (absolute value) that are in temporal coincidence with multiplicity  $m = 2$ .

(iv) the voltage dependence of charge losses and their presence, even for collimated beams ( $10\ \mu\text{m} \times 10\ \mu\text{m}$ ) at the centre of the inter-pixel region, strengthen the idea that charge losses are mainly related to the electron trapping in the inter-pixel region due to the presence of lower electric field.

A novel technique able to correct the charge losses after CSA, for both uncollimated and collimated irradiations, was presented. This approach, exploiting the strong relation between the energy  $E_{\text{CSA}}$  after CSA and the charge-sharing ratio  $R$ , allows the recovery of charge losses and improvements in energy resolution.

An interesting result was also obtained through the analysis of induced-charge pulses with negative polarity created at high energies ( $^{57}\text{Co}$  source). In particular, by summing the absolute value of the energy of the negative pulses with the energy of the coincidence positive pulses (events with multiplicity

$m = 2$ ), it is possible to correct the charge deficit due to hole trapping. We also highlighted the importance of the detection of the negative pulses in order to prevent the presence of false shared events and baseline shifts.

Further measurements at energies higher than 122 keV (e.g. with collimated synchrotron X-ray beams) are foreseen to better understand the results obtained with negative pulses.

Moreover, we foresee to apply the novel correction technique for charge losses on detectors with different electrode layouts (e.g. strips, drift-strips) and at different flux conditions.

### Acknowledgements

The authors would like to acknowledge the technical staff of the laboratory at DiFC of Palermo, Mr Marcello Mirabello for his technical assistance. The authors would also like to acknowledge the technical staff of the interconnect team who performed the bonding of detectors at the Rutherford Appleton Laboratory, Dr Andreas Schneider and Mr Paul Booker.

### Funding information

This work was supported by the Italian Ministry for Education, University and Research (MIUR) under PRIN Project No. 2012WM9MEP, by the Science & Technology Facilities Council (UK) under the Centre for Instrumentation Sensors Managed Programme 2016–2017 and by the Diamond Light Source (proposal MT15047-1).

### References

- Abbene, L. & Gerardi, G. (2015b). *J. Synchrotron Rad.* **22**, 1190–1201.
- Abbene, L., Gerardi, G. & Principato, F. (2013a). *Nucl. Instrum. Methods Phys. Res. A*, **730**, 124–128.
- Abbene, L., Gerardi, G. & Principato, F. (2015a). *Nucl. Instrum. Methods Phys. Res. A*, **777**, 54–62.
- Abbene, L., Gerardi, G., Raso, G., Principato, F., Zambelli, N., Benassi, G., Bettelli, M. & Zappettini, A. (2017). *J. Synchrotron Rad.* **24**, 429–438.
- Abbene, L., Gerardi, G., Turturici, A. A., Del Sordo, S. & Principato, F. (2013b). *Nucl. Instrum. Methods Phys. Res. A*, **730**, 135–140.
- Abbene, L., Gerardi, G., Turturici, A. A., Raso, G., Benassi, G., Bettelli, M., Zambelli, N., Zappettini, A. & Principato, F. (2016). *Nucl. Instrum. Methods Phys. Res. A*, **835**, 1–12.
- Abbene, L., Principato, F., Gerardi, G., Bettelli, M., Seller, P., Veale, M. C., Zambelli, N., Benassi, G. & Zappettini, A. (2018). *J. Synchrotron Rad.* **25**, 257–271.
- Allwork, C., Kitou, D., Chaudhuri, S., Sellin, P. J., Seller, P., Veale, M. C., Tartoni, N. & Veeramani, P. (2012). *IEEE Trans. Nucl. Sci.* **59**, 1563–1568.
- Awadalla, S. A., Al-Grafi, M. & Iniewski, K. (2014). *Nucl. Instrum. Methods Phys. Res. A*, **764**, 193–197.
- Bale, D. S. & Szeles, C. (2008). *Phys. Rev. B*, **77**, 035205.
- Ballabriga, R., Aloyz, J., Campbell, M., Frojdh, E., Heijne, E. H. M., Koenig, T., Llopert, X., Marchal, J., Pennicard, D., Poikela, T., Tlustos, L., Valerio, P., Wong, W. & Zuber, M. (2016). *J. Instrum.* **11**, P01007.
- Barber, W. C., Wessel, J. C., Nygard, E. & Iwanczyk, J. S. (2015). *Nucl. Instrum. Methods Phys. Res. A*, **784**, 531–537.
- Barrett, H. H., Eskin, J. D. & Barber, H. B. (1995). *Phys. Rev. Lett.* **75**, 156–159.
- Benassi, G., Nasi, L., Bettelli, M., Zambelli, N., Calestani, D. & Zappettini, A. (2017). *J. Instrum.* **12**, P02018.

- Bolotnikov, A. E., Bale, D., Butcher, J., Camarda, G. S., Cui, Y., De Geronimo, G., Fried, J., Hossain, A., Kim, K. H., Marshall, M., Soldner, S., Petryk, M., Prokesch, M., Vernon, E., Yang, G. & James, R. B. (2014). *IEEE Trans. Nucl. Sci.* **61**, 787–792.
- Bolotnikov, A. E., Boggs, S. E., Hubert Chen, C. M., Cook, W. R., Harrison, F. A. & Schindler, S. M. (2002a). *Nucl. Instrum. Methods Phys. Res. A*, **482**, 395–407.
- Bolotnikov, A. E., Camarda, G. S., Cui, Y., De Geronimo, G., Eger, J., Emerick, A., Fried, J., Hossain, A., Roy, U., Salwen, C., Soldner, S., Vernon, E., Yang, G. & James, R. B. (2016). *Nucl. Instrum. Methods Phys. Res. A*, **805**, 41–54.
- Bolotnikov, A. E., Camarda, G. C., Wright, G. W. & James, R. B. (2005). *IEEE Trans. Nucl. Sci.* **52**, 589–598.
- Bolotnikov, A. E., Cook, W. R., Harrison, F. A., Wong, A.-S., Schindler, S. M. & Eichelberger, A. C. (1999). *Nucl. Instrum. Methods Phys. Res. A*, **432**, 326–331.
- Bolotnikov, A. E., Cook, W. R., Harrison, F. A., Wong, A.-S., Schindler, S. M. & Eichelberger, A. C. (2002b). *IEEE Trans. Nucl. Sci.* **49**, 270–276.
- Brambilla, A., Ouvrier-Buffet, P., Gonon, G., Rinkel, J., Moulin, V., Boudou, C. & Verger, L. (2013). *IEEE Trans. Nucl. Sci.* **60**, 408–415.
- Brambilla, A., Ouvrier-Buffet, P., Rinkel, J., Gonon, G., Boudou, C. & Verger, L. (2012). *IEEE Trans. Nucl. Sci.* **59**, 1552–1558.
- Budtz-Jørgensen, C. & Kuvvetli, I. (2017). *IEEE Trans. Nucl. Sci.* **64**, 1611–1618.
- Chen, C. M. H., Boggs, S. E., Bolotnikov, A. E., Cook, W. R., Harrison, F. A. & Schindler, S. M. (2002). *IEEE Trans. Nucl. Sci.* **49**, 270–276.
- Chen, H., Awadalla, S. A., Iniewski, K., Lu, P. H., Harris, F., Mackenzie, J., Hasanen, T., Chen, W., Redden, R., Bindley, G., Kuvvetli, I., Budtz-Jørgensen, C., Luke, P., Amman, M., Lee, J. S., Bolotnikov, A. E., Camarda, G. S., Cui, Y., Hossain, A. & James, R. B. (2008). *J. Appl. Phys.* **103**, 014903.
- Chen, H., Awadalla, S. A., Mackenzie, J., Redden, R., Bindley, G., Bolotnikov, A. E., Camarda, G. S., Carini, G. & James, R. B. (2007). *IEEE Trans. Nucl. Sci.* **54**, 811–816.
- Del Sordo, S., Abbene, L., Caroli, E., Mancini, A. M., Zappettini, A. & Ubertini, P. (2009). *Sensors*, **9**, 3491–3526.
- Del Sordo, S., Strazzeri, M., Agnetta, G., Biondo, B., Celi, F., Giarrusso, S., Mangano, A., Russo, F., Caroli, E., Donati, A., Schiavone, F., Stephen, J. B., Ventura, G., Abbene, L., Fauci, F., Raso, G. & Pareschi, G. (2004). *Nuovo Cimento*, **119B**, 257–270.
- Devanathan, R., Corrales, L. R., Gao, F. & Weber, W. J. (2006). *Nucl. Instrum. Methods Phys. Res. A*, **565**, 637–649.
- Eskin, J. D., Barrett, H. H. & Barber, H. B. (1999). *J. Appl. Phys.* **85**, 647–659.
- Frojdth, E., Norlin, B., Thungstrom, G. & Fröjdth, C. (2011). *J. Instrum.* **6**, P02012.
- Gaskin, J. A., Sharma, D. P. & Ramsey, B. D. (2003). *Nucl. Instrum. Methods Phys. Res. A*, **505**, 122–125.
- Gerardi, G. & Abbene, L. (2014). *Nucl. Instrum. Methods Phys. Res. A*, **768**, 46–54.
- Green, F. H., Veale, M. C., Wilson, M. D., Seller, P., Scuffham, J. & Pani, S. (2016). *Phys. Med. Biol.* **61**, 7246–7262.
- Guerra, P., Santos, A. & Darambara, D. G. (2008). *Phys. Med. Biol.* **53**, 1099–1113.
- He, Z. (2001). *Nucl. Instrum. Methods Phys. Res. A*, **463**, 250–267.
- Hong, J., Grindlay, J. E., Chammass, N., Copete, A., Baker, R. G., Barthelmy, S. D., Gehrels, N., Cook, W. R., Burnham, J. A., Harrison, F. A., Collins, J. & Craig, W. W. (2006). *Proc. SPIE*, **6319**, 63190S.
- Iniewski, K. (2014). *J. Instrum.* **9**, C11001.
- Iniewski, K. (2016). *J. Instrum.* **11**, C12034.
- Iniewski, K., Chen, H., Bindley, G., Kuvvetli, I. & Budtz-Jørgensen, C. (2007). *IEEE Nucl. Sci. Symp. Conf. Rec.* **4437135**, 4608–4611.
- Iwanczyk, J., Nygård, E., Meirav, O., Arenson, J., Barber, W. C., Hartsough, N. E., Malakhov, N. & Wessel, J. C. (2009). *IEEE Trans. Nucl. Sci.* **56**, 535–542.
- Kalemci, E. & Matteson, J. L. (2002). *Nucl. Instrum. Methods Phys. Res. A*, **478**, 527–537.
- Kim, J. C., Anderson, S. E., Kaye, W., Zhang, F., Zhu, Y., Kaye, S. J. & He, Z. (2011). *Nucl. Instrum. Methods Phys. Res. A*, **654**, 233–243.
- Knoll, G. F. (2000). *Radiation Detection and Measurement*, ch. 4. New York: John Wiley and Sons.
- Kuvvetli, I. & Budtz-Jørgensen, C. B. (2005). *IEEE Trans. Nucl. Sci.* **52**, 1975–1981.
- Kuvvetli, I. & Budtz-Jørgensen, C. B. (2007). *IEEE Nucl. Sci. Symp. Conf. Rec.* **3**, 2252–2257.
- Marchini, L., Zappettini, A., Gombia, E., Mosca, R., Lanata, M. & Pavesi, M. (2009). *IEEE Trans. Nucl. Sci.* **56**, 1823–1826.
- Mardor, I., Shor, A. & Eisen, Y. (2001). *IEEE Trans. Nucl. Sci.* **48**, 1033–1040.
- Meuris, A., Limousin, O. & Blondel, C. (2009). *Nucl. Instrum. Methods Phys. Res. A*, **610**, 294–297.
- Montémont, G., Lux, S., Monnet, O., Stanchina, S. & Verger, L. (2014). *IEEE Trans. Nucl. Sci.* **61**, 2559–2566.
- Norlin, B., Frojdth, C., Thungstrom, G. & Greiffenberg, D. (2008). *IEEE Nucl. Sci. Symp. Conf. Rec.* **4775083**, 3464–3469.
- Owens, A. & Peacock, A. (2004). *Nucl. Instrum. Methods Phys. Res. A*, **531**, 18–37.
- Ramo, S. (1939). *Proc. IRE*, **27**, 584.
- Schneider, A., Veale, M. C., Duarte, D. D., Bell, S. J., Wilson, M. D., Lipp, J. D. & Seller, P. (2015). *J. Instrum.* **10**, C02010.
- Seller, P., Bell, S., Cernik, R. J., Christodoulou, C., Egan, C. K., Gaskin, J. A., Jacques, S., Pani, S., Ramsey, B. D., Reid, C., Sellin, P. J., Scuffham, J. W., Speller, R. D., Wilson, M. D. & Veale, M. C. (2011). *J. Instrum.* **6**, C12009.
- Sellin, P. J., Prekas, G., Franc, J. & Grill, R. (2010). *Appl. Phys. Lett.* **96**, 133509.
- Shockley, W. (1938). *J. Appl. Phys.* **9**, 635–636.
- Szeles, C., Soldner, S. A., Vydrin, S., Graves, J. & Bale, D. S. (2008). *IEEE Trans. Nucl. Sci.* **55**, 572–582.
- Taguchi, K. & Iwanczyk, J. S. (2013). *Med. Phys.* **40**, 100901-1–100901-19.
- Thomas, B., Veale, M. C., Wilson, M. D., Seller, P., Schneider, A. & Iniewski, K. (2017). *J. Instrum.* **12**, C12045.
- Tomita, Y., Shirayanagi, Y., Matsui, S., Misawa, M., Takahashi, H., Aoki, T. & Hatanaka, Y. (2004). *IEEE Nucl. Sci. Symp. Conf. Rec.* **6**, 3733–3737.
- Veale, M. C., Bell, S. J., Duarte, D. D., Schneider, A., Seller, P., Wilson, M. D. & Iniewski, K. (2014). *Nucl. Instrum. Methods Phys. Res. A*, **767**, 218–226.
- Veale, M. C., Bell, S. J., Jones, L. L., Seller, P., Wilson, M. D., Allwork, C., Kitou, D., Sellin, P. J., Veeramani, P. & Cernik, R. C. (2011). *IEEE Trans. Nucl. Sci.* **58**, 2357–2362.
- Xu, C., Danielsson, M. & Bornefalk, H. (2011). *IEEE Trans. Nucl. Sci.* **58**, 614–625.
- Zappettini, A., Zha, M., Marchini, L., Calestani, D., Mosca, R., Gombia, E., Zanotti, L., Zanichelli, M., Pavesi, M., Auricchio, N. & Caroli, E. (2009). *IEEE Trans. Nucl. Sci.* **56**, 1743–1746.
- Zhang, F., He, Z. & Seifert, C. E. (2007). *IEEE Trans. Nucl. Sci.* **54**, 843–848.
- Zhu, Y., Anderson, S. E. & He, Z. (2011). *IEEE Trans. Nucl. Sci.* **58**, 1400–1409.